Carboxylate Ligands-Promoted Superior Electrocatalytic Performance for Oxygen Evolution Reaction and Their Mechanisms

Chengfei Li
Sun Yat-sen University
Jia-Wei Zhao
Sun Yat-sen University
Ling-Jie Xie
Sun Yat-sen University
Jin-Qi Wu
Sun Yat-sen University
Qian Ren
Sun Yat-sen University
Yu Wang
Sun Yat-sen University
Gao-Ren Li (ligaoren@mail.sysu.edu.cn)
Sun Yat-sen University https://orcid.org/0000-0002-9222-7274

Article

Keywords: Metal-organic frameworks, Carboxylate ligands, Oxygen evolution reaction, Electrocatalysis, NiFe LDHs

Posted Date: February 8th, 2021

DOI: https://doi.org/10.21203/rs.3.rs-154877/v1

Abstract

Metal-organic frameworks (MOFs) with carboxylate ligands as co-catalysts are very efficient for oxygen evolution reaction (OER). However, the role of local adsorbed carboxylate ligands around the in situ transformed metal (oxy)hydroxides during OER is often overlooked. Here we reveal the extraordinary role and mechanism of surface adsorbed carboxylate ligands on bi/trimetallic layered double hydroxides (LDHs)/MOFs for OER catalytic activity enhancement. The results of X-ray photoelectron spectroscopy (XPS), synchrotron X-ray absorption spectroscopy and theoretical calculations show that the carboxylic groups around metal (oxy)hydroxides can efficiently induce the interfacial electron redistribution, facilitate abundant high-valence state of nickel species with partial distorted octahedral structure, and optimize the d-band center together with the beneficial Gibbs free energy of intermediate. Furthermore, the results of in-situ Raman and FI-IR spectra firstly reveal that the surface adsorbed carboxylate ligands as Lewis base can promote the sluggish OER kinetics by accelerating proton transfer and facilitating adsorption/ activation/dissociation of hydroxyl ions (OH^-). Our findings will offer unique insights into the reason for disclosing the origin of excellent electrocatalytic activity for MOF/NiFe-LDHs catalysts.

Introduction

The oxygen evolution reaction (OER) is a critical process in the efficient energy conversion and storage electrochemical systems, such as water splitting and metal-air batteries.[1,2] Unfortunately, greatly sluggish multistep proton-coupled electron transfer during OER results in high overpotential and low efficiency.[3] Recently, huge efforts have been devoted to preparing many non-noble metal electrocatalysts to improve OER efficiency and lower the cost of catalysts.[4,5] Among them, the metal-organic frameworks (MOFs), constructed by strong coordination bonds between organic ligands and metal nodes/clusters with periodic structural units, have attracted great attentions due to the advantages of homogeneous and heterogeneous electrocatalysts, highly exposed molecular metal sites and large specific surface area for OER.[6]

However, to date, many studies mainly focused on the hypothesis that the enhancement of OER catalytic performance is mainly attributed to the coupled effects of heterometals,[7,8] coordination unsaturation of metal sites and/or conductivity improvement.[9,10] For example, Zhao,[11] Zhu,[12] Qiao[13] and Liu[14] groups have prepared two-dimensional ultrathin MOF nanosheets as OER electrocatalyst, and their remarkably catalytic activity is attributed to be one of the coordinatively unsaturated and intrinsic molecular metal sites, lattice strain and synergistic effects between the different metals. Despite these conclusions have been confirmed by experimental results and DFT calculations, the role of electron-rich functional group (typical carboxyl group) of organic ligand is always overlooked in the enhanced OER catalytic performance. That is, how does the electron-rich functional group affect the electronic structure of active site, transfer/activation/ dissociation of OH^- species, and the relationship of functional carboxylate ligands (CLs)-performance are still ambiguous. As we all known, the coordination environment of electroactive center can be tailored through the negatively-charged coordinated groups or nonmental

atoms, which can optimize the binding energies of intermediates via the appropriate d-band center.[11–16] In addition, the CLs as promoters from amino-acid resides of protein backbones can help to act as an internal base for proton transfer by the form of hydrogen bond with coordinated water.[17,18] Thus, inspired by above studies, we wonder if there are similar functions of transfer/activation/dissociation behaviors of OH^- species from the CLs in MOF or extra addition of CLs in electrolyte. However, the above situation is often ignored during the investigation of the origin of superior electrocatalytic property of MOF catalysts.[19–22] Therefore, unveiling the catalytic performance enhancement promoted by CLs is urgent, which is very important for efficient understanding of catalytic mechanisms and thus rational design of efficient OER electrocatalysts.

In this study, we detailedly elucidate the important role of electron-rich carboxylic groups from either the interior MOF or the extra addition of CLs on the improved OER electrocatalytic activity (Scheme 1). To reveal the promotion effect of CLs on catalytic activity, OER catalytic performance of NiFe-LDHs was first measured with and without CLs on their surface for the comparisons. The remarkably enhanced OER catalytic activity of NiFe-LDHs/CLs can be attributed to the electron redistribution together with the optimized Gibbs free energies of intermediates, evidenced by X-ray photoelectron spectroscopy (XPS), synchrotron X-ray absorption spectroscopy (XAS) and DFT theoretical calculations. Furthermore, the stable CLs in MOFs provided an ideal platform for exploring the effect of internal CLs on catalytic performance. The results of in-situ Raman and FT-IR spectroscopy both show that the negatively charged CLs can be well utilized as a proton transfer mediator and cocatalyst, that is, promote transportation, activation and dissociation of hydroxyls resulting in fast reaction kinetics and low overpotential.

Results

Here transition metal-LDHs catalysts are firstly taken as research models to interpret the great important role of CL on promoting OER catalytic performance (The surface morphologies of various transition metal-LDHs are shown in Figure S1). The OER catalytic activity of various transition metal-LDHs catalysts were tested with and without CLs as shown in Fig. 1a-h. Obviously, with CLs on the surface, CoV-LDHs, CoFe-LDHs, NiFeMn-LDHs, NiCu-LDHs, NiCo-LDHs, NiFe-LDHs, NiMn-LDHs and NiV- LDHs all show remarkably enhanced OER catalytic activity, and the overpotentials of above transition metal-LDHs without CLs drop evidently. The above result implies that the promotion effect of CLs for OER catalytic activity is universal for bi/trimetallic LDHs catalysts. In order to avoid decentralization, the analysis and discussion in this paper mainly focuses on NiFe-LDHs. Here the OER reaction kinetics were investigated by electrochemical impedance spectroscopy (EIS) and Tafel slop as shown in Fig. 2, which exhibits the obviously promoted OER kinetics by CLs. Specifically, compared with that of NiFe- LDHs (247.2 Ω of R_{ct}), the NiFe-LDHs/CLs own a smaller charge transfer resistance (199.9 Ω of R_{ct}) (Figue 2a), indicating that CLs can markedly facilitate the charge transfer during OER, further evidenced by the Tafel slope values (Figue 2b). Notably, when the overpotential is low, a small Tafel slope of 89 mV dec^{-1} is obtained for

NiFe-LDHs/CLs, and it is smaller than that of pure NiFe-LDHs (98 mV dec^{-1}). However, when the overpotential is high, NiFe-LDHs/CLs displays a much smaller Tafel slope (158 mV dec^{-1}) and much faster reaction dynamics than NiFe-LDHs (223 mV dec^{-1}), indicating that the CLs as a transfer mediator can facilitate the transfer rate of protons. This is consistent with previously reported works.[17–18,23–24] This is also in line with the OER catalytic activity displayed in the polarization curve. The enhanced intrinsic activity of catalyst is also important for excellent OER performance. As shown in Fig. 2c, the anodic current density of NiFe-LDHs increased dramatically after extra addition of CLs in electrolyte, and NiFe-LDHs/CLs exhibited a low overpotential of 337 mV at a current density of 10 mA cm^{-2}, which is lower than that of NiFe-LDHs (357 mV), suggesting the remarkable catalytic activity promoted by CLs. Additionally, we explored the remarkable effect of soaking time in CLs-containing electrolyte on catalytic performance, that is, the influence of CLs loading on the catalyst surface on the enhanced OER catalytic performance (Fig. 2d). Obviously, the coordinated CLs can tailor the OER activity through different CL loadings adsorbed on catalysts. Also, the effects of different concentrations of CLs in electrolyte were investigated as shown in Fig. 2e. When the concentration of CLs is 0.10 M for 15 min, the best catalytic performance is achieved. In addition, the coordinated CLs on the surface of catalyst have been detected by Fourier transform infrared (FT-IR) spectroscopy (Fig. 2f). The peak at 1088 cm^{-1} can be attributed to γ(OH) bending vibrations of $^{-}$OH–OOC–*Ar* (*Ar*: benzene ring), indicating a proton transfer mediator via the form of hydrogen oxygen bond.[25] Two peaks at 1576 and 1498 cm^{-1} are clearly seen and are ascribed to ν_{as}(–COO–) and ν_{s}(–COO–) of carboxylate,[26] respectively. Notably, the peak at 1668 cm^{-1} corresponds to the bending vibrations of –COO–,[27] demonstrating the existence of CLs. Compared with the peak of metal-oxygen bonds of NiFe-LDHs, a strong and shifted peak appears at ~ 500 cm^{-1} for NiFe-LDHs/CLs, indicating a coordination between Ni/Fe metal sites and CLs.[28]

The above results lead us to think about why and how do CLs promote OER electrocatalytic activity of NiFe-LDHs or other catalysts. Herein, a series of DFT calculations were conducted to further answer this question. Considering the adsorbed form of CLs on the interfaces of catalyst, there are three theoretical models were studied including physical level adsorption (PLA) model (denoted as NiFe-LDHs/CLs-PLA, Figure S2), physical vertical adsorption (PVA) model (denoted as NiFe-LDHs/CLs-PVA, Figure S3), and chemical vertical adsorption (CVA) model (denoted as NiFe-LDHs/CLs-CVA, Figure S4). In the first two models, the CLs are not directly bonded with the interfacial metal atoms and their states are similar, while in the third model, the CLs coordinate with metal atoms. For the convenience of discussion, here we only choose NiFe-LDHs/CLs-PVA and NiFe-LDHs/CLs-CVA models for the comparative studies. Firstly, the interfacial charge distribution in hybrid system was elucidated in above two models. From the differential charge density, Fig. 3a exhibits no interaction among electrons at the interfaces in NiFe-LDH/CL-PVA model, while NiFe-LDH/CLs-CVA model shows electron transfer from CLs to Ni atoms at near interface (Fig. 3b), and the adjacent Ni atom shows partial electron donation. This result points out that the CLs can modify the catalyst only in the case of bond formation. Impressively, the d band center model would be a good descriptor of the adsorbate–metal interaction. As shown in Fig. 3c and 3d, the d-band center (E_d) of NiFe-LDHs/CLs-CVA model is far away from the Fermi level from − 2.73 to -3.42 eV after the

chemisorption of CLs, and the down-shift of d band center will increase the bonding states and decrease the anti-bonding states, and thus will weaken bonding strength of intermediates,[29] and accordingly will enhance the catalytic performance of OER. But the E_d of NiFe-LDHs/CLs-PVA displays almost no little change. Furthermore, the Gibbs free energy (ΔG) of intermediate species, as a key descriptor of OER activity, has been demonstrated to be obviously decreased (Fig. 3e and Figure S5), including adsorption (step *i*), dissociation (steps *ii* and *iii*) and desorption (step *iv*). Interestingly, all the Gibbs free energy of OER intermediates for NiFe-LDHs/CLs are obviously lower than those of NiFe-LDHs and NiFe-LDHs/ CLs-PVA model. Specifically, lower ΔG value of step *i* of NiFe-LDHs/CLs-CVA model implies stronger adsorption of OH^- compared with those of NiFe-LDHs and NiFe-LDHs/CLs-PVA model, benefiting for the initiation of OER. Importantly, the theoretical overpotentials of NiFe-LDHs/CLs-CVA model is only 370 mV, which is much lower than those of NiFe-LDHs (590 mV) and NiFe-LDHs/CLs-PVA model (600 mV). The above results demonstrated that the CLs can optimize adsorption strength of OER intermediates, and especially can lower reaction energy barriers from optimal E_d to promote the catalytic activity.

To gain in-depth insight into how the adsorbed CLs promote catalytic activity, the interfacial electronic behavior of NiFe-LDHs/CLs was also investigated via concrete experimental characterizations. X-ray photoelectron spectroscopy (XPS) and X-ray absorption spectroscopy (XAS) can be adopted to explore the synergistic electronic effect between CLs and in situ-formed metal (oxy)hydroxides on the surface of NiFe-LDHs. As shown in Fig. 4a, compared with that of the initial NiFe-LDHs, XPS peak of Ni $2p_{3/2}$ at 857.6 eV for post-OER NiFe-LDHs displays the oxidation of partial Ni^{2+} into Ni^{3+}. More importantly, the peak of Ni $2p_{3/2}$ of post-OER NiFe-LDHs/CLs shifts to positive binding energy of 857.9 eV, suggesting that the partial electrons are transferred from a neighboring Ni to O/Fe, consistent with differential charge data analysis. In addition, the ratio of Ni^{3+} $2p_{3/2}$ /Ni^{2+} $2p_{3/2}$ of post-OER NiFe-LDHs/CLs jumped to a high value (0.79) compared with that of post-OER NiFe-LDHs (0.64), suggesting the enriched superficial oxyhydroxides transformation of metal sites during the electrochemical activation. The above results reveal the fact that the enriched Ni^{3+} on the surface of post-OER NiFe-LDHs/CLs was responsible for OER activity enhancement, consistent with previously reported works.[30] In contrast, the fitted peak of Fe^{3+} $2p_{3/2}$ of post-OER NiFe-LDHs/CLs shifts to low binding energy of 712.7 eV compared with that of post-OER NiFe-LDHs (712.9 eV) and NiFe-LDHs (713.2 eV) (Fig. 4b). The above results mainly originate from carboxyl oxygen coordinated with Ni/Fe sites that tailors interfacial electron redistribution and charge state and thus induces downshift of metal d-band to penetrate p-band of oxygen intermediates (Figure S6),[31] which is in agreement well with the result of DFT calculations. This phenomenon can be well elucidated in term of coordinated oxygen from ligand strengthening electron interactions between Ni and Fe (Fig. 4c). The t_{2g} d-orbitals of Ni^{2+} in the low-spin state are fully occupied, resulting in $e^- - e^-$ repulsion between the bridging O^{2-} and Ni^{2+}.[32] For Fe^{3+}, $3d^5$ valence electron configuration with unpaired electrons in the π-symmetry (t_{2g}) d-orbitals implies a weak interaction via π-donation.[33] Thus, to keep the balance, the electron interactions between Fe^{3+} and Ni^{2+} can well be strengthened via bridging O^{2-} after more oxygen coordination. As such, the partial charge transfer from Ni^{2+} to Fe^{3+} will be easily occurred, and

this has been proven by the shift of binding energy of Ni^{2+} $2p_{3/2}$ of post-OER NiFe-LDHs/ CLs. As a consequence, there are more empty orbitals at Ni 3d e_g energy level and more electrons at Fe 3d t_{2g} energy level after the introduction of local ligand environment.[34] Furthermore, the normalized X-ray absorption spectra was utilized to study the fine structure of NiFe-LDHs, post-OER NiFe-LDHs and post-OER NiFe-LDHs/CLs as shown Fig. 4d-g. Specifically, an obvious shift of Ni K-edge XANES adsorption-edge to a higher energy is seen for post-OER NiFe-LDHs/CLs compared with those of NiFe- LDHs and post-OER NiFe-LDHs, indicative of increased charge state of Ni (Fig. 4d), consistent with XPS analysis results. In addition, the mild decline of Fe valence state after CLs adsorption can also be verified by the shift of Fe adsorption-edge (Fig. 4e). Moreover, the Fourier transform (FT) of extended X-ray absorption fine structure (EXAFS) spectra at Ni K-edge implies the dominant peak at 1.6 Å is ascribed to Ni/Fe–O bond, and the relatively weak peaks at 2.7 Å is associated with Ni–Ni(Fe) bonds (Fig. 4f). Interestingly, we note that the Ni–O bond length slightly becomes shorter by 0.2 Å, and simultaneously, the Ni–Ni/Fe bond length becomes longer, suggesting the presence of lattice strain under CLs coordination.[14,34] The result further demonstrates that the CLs can regulate the interatomic distances and induce the partial distorted structure, and meanwhile alter the electronic structures of active sites that could help to optimize the intrinsic activity.[35–36] Similarly, in Fig. 4g, FT-EXAFS curves at Fe K-edge shows the similar shifts of Fe-O and Fe-Ni/Fe bond lengths. Such above peak shifts could be further understood by a slight local distortion of the octahedral coordination of Fe/Ni,[37] which is closely related to e_g/t_g orbits of the active sites that strongly affect the adsorption strength of intermediates.[38]

Inspired by the high catalytic performance promoted by the additional CLs on the surface of catalysts, we presume that if the catalyst itself contains CLs, what will the promoting effect be like? Typically, metal-organic framework material with CLs as OER catalyst were systemically explored, because most of studies mainly focused on the synergistic effect between metals or lower coordinated metals and so on, always ignoring the effect of local ligand environments on the catalytic performance improvement. With this thinking, NiFeMn trimetal-organic frameworks (NiFeMn-MOFs) was chosen as our research model, because CLs in NiFeMn-MOFs are relatively stable, which is critical key for unveiling the roles of CLs at the atomic level on OER activity. Corresponding evidences for confirming stability of CLs in hybrid system, including the crystal structure, morphology, surface electronic feature, and functional groups of NiFeMn-MOFs before and after cycling test have been analyzed as shown in Figure S7-12. The OER activity of NiFeMn-MOFs was also evaluated in a conventional three-electrode cell containing 1.0 M KOH solution at a scan rate of 5 mV s^{-1}. For comparison study, the different contents of CLs in post-OER NiFeMn-MOFs-*x* min toward OER activity were investigated (*x* = 5, 10 and 15, *x* represents the soaking time for post-OER NiFeMn-MOFs in 6.0 M KOH). The concentration of CL increases in electrolyte with soaking time increasing, evidenced by the UV-vis spectroscopy in Fig. 5a. This result means that the residual CLs in the frameworks will decrease through metal cations transforming into (oxy) hydroxides (Figure S10f).[39] Strikingly, NiFeMn-MOFs exhibit a high catalytic activity with a low overpotential of 253 mV at the current density of 10 mA cm^{-2} (Fig. 5b), which is 9, 17 and 18 mV less than those of post-OER NiFeMn-MOFs-5 min, post-OER NiFeMn-MOFs-10 min, post-OER NiFeMn-MOFs-15 min, respectively,

suggesting that the CLs can modulate catalytic activity of OER. Impressively, NiFeMn-MOFs demonstrated a remarkably fast reaction kinetics with a low Tafel slop value of 41 mV dec^{-1} (Fig. 5c), which is 2.7, 5.0 and 5.2 times lower than those of post-OER NiFeMn-MOFs-5 min, post-OER NiFeMn-MOFs-10 min, post-OER NiFeMn-MOFs-15 min, respectively. In addition, the electrochemical impedance spectroscopy (EIS) was performed to explore interfacial reactions and OER kinetics (Figure S13). Notably, an ultrasmall semicircle at low-frequency region associated with the mass diffusion process for NiFeMn-MOF compared with other samples can be observed, demonstrating a stronger adsorption/desorption of reaction intermediates (such as OH^-) on the surface of catalyst.[40] Moreover, the value of charge transfer resistance (R_{ct}) for NiFeMn-MOFs (0.76 Ω) is smaller than those of post-OER NiFeMn-MOFs-5/10/15 min samples (0.81, 1.03 and 1.06 Ω, respectively), indicating fast electron transport migration between the solution and electrode interface.

To insight into how CLs promote reaction kinetics, OH activation/dissociation that strongly determine fast kinetics were investigated via in situ Raman, FT-IR spectroscope, pH-dependent and deuterium kinetic isotope effects (KIEs). It is well known that Lewis bases (SO_4^{2-}/PO_4^{3-}/COO^-/CO_3^{2-}/SeO_4^{2-}) in solution are a proton acceptor,[41] which can be utilized as a transfer station for protons to facilitate the proton transmission rate, evenly perform the functions of OH activation and dissociation. To verify above hypothesis and explain why NiFeMn-MOF possesses a remarkably superior reaction kinetics, in situ Raman measurement was firstly carried out. As shown in Fig. 6a, potential-dependent in situ Raman spectroscopy displays the structure evolution during OER. With potential increasing, the strong signals of C-COOH (308 cm^{-1}),[42] COO^- (1402 cm^{-1}),[43] COOH (1683 cm^{-1}),[23, 42] and free OH^- (924 cm^{-1})[44] can be detected, nevertheless in ex situ spectrum, all above signals of various groups disappear (Figure S14), indicating the real process of proton transfer mediator via the form of $-COO-HO^-$, and subsequent adsorption/activation/dissociation of OH^-, consistent with previously reported works.[23] Specifically, as schematically illustrated in Fig. 6b, the free OH^- from bulk electrolyte firstly react with interfacial coordinatively unsaturated *Ar*-COO^- in form of *Ar*-$COO-HO^-$, accelerating the rate of proton transfer (Step 1: proton transfer station). Secondly, the O atom from *Ar*-$COO-HO^-$ transfers to metal site to form *Ar*-COO–HO* (* denotes as the active site), and followed by the activation and dissociation (Step 2), namely, another OH^- from electrolyte will react with H of *Ar*-COO–HO* to produce adsorbed O* intermediate. Meanwhile the proton transfer continues to form *Ar*-$COO-HO^-$ (Step 2). Thirdly, another OH^- from *Ar*-$COO-HO^-$ will bond with O* intermediate to form *Ar*-COO–HOO* under applying potential (Step 3). Similarly, under the role of activation and dissociation of carboxylic group, the *Ar*-COO–HOO* will be deprotonated via OH^-/COO coupled reaction to form *Ar*-COO–H(OO*)–OH, and subsequently produce oxygen molecular and water (Steps 4 and 5). The above process of transfer/ activation/dissociation of hydroxyls realizes remarkable catalytic activity of NiFeMn-MOF. Additionally, the step of proton transfer was further confirmed by in situ FT-IR spectroscope (Fig. 6c). Compared with that of initial NiFeMn-MOFs, two peaks at 1642 and 1057 cm^{-1} in Fig. 6c can be attributed to carboxyl group[23,27,43,45,47] and hydroxyl group[25], respectively, appeared during OER, and become stronger with potential increasing, indicating the uncoordinated carboxylate provided the extra hydrogen site as a proton transfer bridge. Furthermore, the

study of pH dependence can provide useful insight on the kinetics and intermediates of the reaction. As shown in inset of Fig. 6d and 6e, the pH-dependent value range is 0.6 for NiFeMn-MOFs, and the slop of change is ~ 2.5 times lower than that of NiFeMn-LDHs, suggesting negligible pH-dependent OER kinetics for NiFeMn-MOFs and higher intrinsic activity with help proton transfer mediator. Moreover, it is known that deuterium KIEs can reflect proton transfer and dissociation, and thus will help to verify above described catalytic processes. As shown in Fig. 6f and 6g, the existence of KIEs demonstrated proton transfer involved in OH^-/OD^- dissociation, which affects the OER reaction rate. Obviously, the LSV curve of NiFeMn-MOFs in a 1.0 M $NaOH/H_2O$ solution exhibits much higher current density compared with NiFeMn-MOFs in 1.0 M $NaOD/H_2O$ solution by a factor of 6 at the initial stage, but quickly decreases with the potential increasing, suggesting fast cleavage of O – H bonds. However, the KIEs value of NiFeMn-LDHs shows a larger primary isotope effects in the absence of CLs, strongly proving that superior kinetics derived from the CLs that can help handling the proton transfer and dissociation on the surface of catalyst.

Discussion

In summary, we have presented the vital promotion of extrinsic-internal adsorbed CLs on OER activity. By adding CLs to the alkaline electrolyte, NiFe-LDHs and other bimetallic LDHs demonstrate obviously catalytic activity enhancement and fast reaction kinetics. DFT calculations have confirmed that the origin of enhanced electrocatalytic performance was originated from the electron redistribution at the interface of oxyhydroxides/CLs, and thus induced the downshift of d-band center to optimize the binding strength of intermediates. XPS and XAS measurements further validated the interfacial electronic behaviors and partial distorted structure under the role of surface-adsorbed CLs. Furthermore, taking the NiFeMn-MOFs as a research model of inherent CLs, the potential-dependent in situ Raman and FT-IR spectroscopy firstly revealed the reason of the promotion of fast reaction kinetics, which is attributed to that the CLs as Lewis base can facilitate transmission/adsorption/activation/dissociation of OH^-. This work not only reveals the critical role of local coordinated CLs, but also provides the new insights into the engineering of exterior coordination environments of catalysts to promote intrinsic catalytic activity and reaction kinetics for OER.

Methods

Synthesis of the NiFe-LDHs

Firstly, 0.6 mmol $Ni(NO_3)_2{\cdot}6H_2O$, 0.2 mmol $Fe(NO_3)_3{\cdot}9H_2O$, 3 mmol CH_4N_2O, and 3 mmol NH_4F were dissolved in 30 mL deionized water. Secondly, the mixed solutions were placed into a 45 mL-stainless-steel Teflon-lined autoclave maintained at 140°C for 4 h. After natural cooling to room temperature, the resultant NiFe-LDH/NF were washed thoroughly with deionized water and dried in vacuum at 60°C for 12 h.

Synthesis of CoV-LDHs

The CoV-LDHs were synthesized with similar above process, except that 0.6 mmol $Ni(NO_3)_2{\cdot}6H_2O$ and 0.2 mmol $Fe(NO_3)_3{\cdot}9H_2O$ were replaced by 0.6 mmol $Co(NO_3)_2{\cdot}6H_2O$ and 0.2 mmol VCl_3, respectively .

Synthesis of CoFe-LDHs

The CoFe-LDHs were synthesized with similar above process, except that 0.6 mmol $Ni(NO_3)_2{\cdot}6H_2O$ was replaced by 0.6 mmol $Co(NO_3)_2{\cdot}6H_2O$.

Synthesis of NiFeMn-LDHs

The NiFeMn-LDHs were synthesized with similar above process, except that 0.1 mmol $MnCl_2{\cdot}4H_2O$ was extra added.

Synthesis of NiCu-LDHs

The NiCu-LDHs were synthesized with similar above process, except that 0.2 mmol $Fe(NO_3)_2{\cdot}6H_2O$ was replaced by 0.2 mmol Cu $(NO_3)_2{\cdot}3H_2O$.

Synthesis of NiCo-LDHs

The NiCo-LDHs were synthesized with similar above process, except that 0.2 mmol $Fe(NO_3)_2{\cdot}6H_2O$ was replaced by 0.2 mmol Co $(NO_3)_2{\cdot}6H_2O$.

Synthesis of NiMn-LDHs

The NiCo-LDHs were synthesized with similar above process, except that 0.2 mmol $Fe(NO_3)_2{\cdot}6H_2O$ was replaced by 0.2 mmol Mn $(NO_3)_2{\cdot}6H_2O$.

Synthesis of NiV-LDHs

The NiV-LDHs were synthesized with similar above process, except that 0.2 mmol $Fe(NO_3)_2{\cdot}6H_2O$ was replaced by 0.2 mmol VCl_3.

Synthesis of NiFeMn-MOFs: 0.12 mmol $Fe(NO_3)_3{\cdot}9H_2O$, 0.54 mmol $Ni(NO_3)_2{\cdot}6H_2O$, 0.06 mmol $MnCl_2{\cdot}4H_2O$ and 100 mg terephthalic acid were dissolved in a 30 mL of mixture solution of DMF/ethanol/water (v:v:v = 12.5:1.5:1.5). After continuously stirring for 30 min, the solution and the cleaned Ni foam (2.8*3*0.5) were transferred into a 45 mL Teflon-lined autoclave. Subsequently, the autoclave maintained at 125°C for 12 h in an oven. After naturally cooling down to room temperature, the brown red MIL-53(NiFe)/Ni foam was taken out, and washed with deionized H_2O for several times, and finally dried at 60°C overnight for further characterization.

Synthesis of NiFe-MOFs

The NiFe-MOFs were synthesized with similar above process, except that 0.06 mmol $MnCl_2 \cdot 4H_2O$ was not added.

Physical Characterizations. TEM image and EDS were obtained on JEOL JEM-1400 at 300 kV. SEM measurement was carried out on a Quanta 400FEG instrument. X-ray diffraction (XRD) patterns of as-prepared samples were recorded on a Rigaku SmartLab diffractometer with Cu Kα (λ = 1.5406 Å) radiation operating at 30 kV and 200 mA. X-ray photoelectron spectroscopy (XPS) measurements were performed on an ESCA Lab250 X-ray photoelectron spectrometer. Fourier Transform infrared (FT-IR) spectra were conducted on the FT-IR instrument (EQUINOX 55). The UV-visible spectroscopy was collected with UV-Vis-spectrophotometer (UV-Vis, Shimadzu UV-2450).

XAFS measurements

The X-ray absorption find structure spectra (Ru K-edge) were collected at 1W1B station in Beijing Synchrotron Radiation Facility (BSRF). The storage rings of BSRF were operated at 2.5 GeV with an average current of 250 mA. Using Si (111) double-crystal monochromator, the data collection was carried out in transmission/ fluorescence mode using ionization chamber. All spectra were collected in ambient conditions.

Electrochemical Measurements

The linear sweep voltammograms (LSVs) were performed on an electrochemical station (CHI 760E) in a three-electrode cell with 1.0 M KOH solution. The as-prepared samples were used as working electrode, graphite rod was utilized as counter electrode and Hg/HgO electrode was used as reference electrode. The LSV measurement was performed at a scan rate of 5 mV s^{-1} unless otherwise stated. All the measured potentials were converted to reversible hydrogen electrodes (RHE) according to $E_{RHE} = E_{Hg/HgO} + 0.059\ pH + 0.098$ V. The LSV measurements were performed at a scan rate of 5 mV s^{-1}. All the polarization measurements were not corrected with iR compensation. Electrochemical impedance spectroscopy (EIS) measurements were studied in a frequency range from 100 KHz to 100 mHz.

Theoretical Computational Methods:

Spin-polarized density functional theory (DFT) calculations were performed in the plane wave and USPP as implemented in Quantum ESPRESSO.[1] Adsorption energies were calculated with Perdew–Burke–Ernzerhof exchange functional correction.[2] The effective U-J terms, from linear response theory,[3] were 3.5 and 6.6 for Fe and Ni, respectively. The kinetic energy cutoffs of 25 Ry and 225 Ry were chosen for the wave functions and augmented charge densities. All the atomic structures for the models were fully relaxed with self-consistency criteria of 10^{-5} Ry and all atomic coordinates were converged to within 10^{-3} Ry/bohr for maximal components of forces. The occupancy of the one-electron states was calculated using an electronic temperature of k_BT=0.01 Ry for surfaces and 10^{-3} Ry for molecules in vacuum. All energies were extrapolated to T = 0 K. Vacuum slab of 12 Å was used for surface isolation to prevent

interaction between two surfaces. Reciprocal space was sampled by the Γ-centered Monkhorst-Pack scheme with (lattice parameters × k) ~ 30.

The OER free energy profiles were derived using the same scheme utilized in previous studies.[4]

The theoretical overpotential at which the step becomes downhill may be calculated as:

$$\eta = \frac{max(\Delta G_1, \Delta G_2, \Delta G_3, \Delta G_4)}{e} - 1.23\ [V]$$

The OER mechanism contains four elementary steps, and each of these steps contains a single proton-electron transfer, shown as the following:

$$* + H_2O \rightarrow HO* + e^- + H^+$$

$$HO* \rightarrow O* + e^- + H^+$$

$$O* + H_2O \rightarrow HOO* + e^- + H^+$$

$$HOO* \rightarrow * + O_2 + e^- + H^+$$

The free energy of each adsorbate is calculated at 0 V *vs.* RHE by referencing to liquid water and hydrogen gas at standard conditions. The correction calculated using the harmonic approximation for every adsorbate and surface, with typical values of +0.05 eV, +0.35 eV, +0.40 eV for O*, HO* and HOO*, respectively.

Declarations

Competing interests:

The authors declare no competing interests.

Author contributions

C.F.L. and G.R.L designed the experiments and performed the analysis of the whole data and wrote the paper. J.W.Z. performed DFT calculations and data analysis. L.J.X., J.Q.W., Q.R., and Y.W. conducted relative measurements and data analysis.

Acknowledgements

This work was supported by National Basic Research Program of China (2016YFA0202603), NSFC (21821003, 91645104), Natural Science Foundation of Guangdong Province (S2013020012833 and 2016A010104004), Guangdong Basic and Applied Basic Research Foundation (2019A1515111033),

China Postdoctoral Science Foundation (2020M672934), Fundamental Research Funds for the Central Universities, Sun Yat-sen University (20lgpy88).

References

1. Qian, Q. *et al*. Ambient fast synthesis and active sites deciphering of hierarchical foam- like trimetal-organic framework nanostructures as a platform for highly efficient oxygen evolution electrocatalysis. *Adv Mater.* **31,** 1901139 (2019).
2. Chen, G. *et al*. Efficient and stable bifunctional electrocatalysts Ni/Ni_xMy (M= P, S) for overall water splitting. *Adv. Funct. Mater.* **26,** 3314-3323 (2016).
3. Chen, G. *et al*. Accelerated hydrogen evolution kinetics on NiFe-layered double hydroxide electrocatalysts by tailoring water dissociation active sites. *Adv Mater.* **30,** (2018).
4. Zhuang, L. *et al*. A surfactant-free and scalable general strategy for synthesizing ultrathin two-dimensional metal-organic framework nanosheets for the oxygen evolution reaction. *Angew. Chem. Int. Ed.* **58,** 13565-13572 (2019).
5. Zhao, M. *et al*. Ultrathin 2D metal-organic framework nanosheets. *Adv. Mater.* **27,** 7372-7378 (2015).
6. Zhu, D. *et al*. Engineering 2D metal-organic framework/MoS_2 interface for enhanced alkaline hydrogen evolution. *Small* ***15,*** 1805511 (2019).
7. Li, F. L. *et al*. Nanoscale trimetallic metal-organic frameworks enable efficient oxygen evolution electrocatalysis. *Angew. Chem. Int. Ed.* **130,** 1906-1910 (2018).
8. Zhou, W. *et al*. Stable hierarchical bimetal–organic nanostructures as highperformance electrocatalysts for the oxygen evolution reaction. *Angew. Chem. Int. Ed.* **58,** 4227-4231 (2019).
9. Li, J. *et al*. Low-crystalline bimetallic metal-organic framework electrocatalysts with rich active sites for oxygen evolution. *ACS Energy Lett.* **4,** 285-292 (2018).
10. Tan, J. *et al*. Fe doped metal organic framework (Ni)/carbon black nanosheet as highly active electrocatalyst for oxygen evolution reaction. *Int. J. Hydrog. Energy.* **45,** 21431-21441 (2020).
11. Duan, J. *et al*. Ultrathin metal-organic framework array for efficient electrocatalytic water splitting. *Nat. Commun.* ***8,*** 1-7 (2017).
12. Zhuang, L. *et al*. A surfactant-free and scalable general strategy for synthesizing ultrathin two-dimensional metal–organic framework nanosheets for the oxygen evolution reaction. *Angew. Chem. Int. Ed.* **131,** 13699-13706 (2019).
13. Zhao, S. *et al*. Ultrathin metal–organic framework nanosheets for electrocatalytic oxygen evolution. *Nat. Energy.* **1,** 1-10 (2016).
14. Cheng, W. *et al*. Lattice-strained metal–organic-framework arrays for bifunctional oxygen electrocatalysis. *Nat. Energy.* **4,** 115-122 (2019).
15. Cheng, W. *et al*. NiMn-based bimetal-organic framework nanosheets supported on multi-channel carbon fibers for efficient oxygen electrocatalysis. *Angew. Chem. Int. Ed.* **59,** 18234-18239 (2020).

16. Li, P. *et al*. Tuning electronic structure of NiFe layered double hydroxides with vanadium doping toward high efficient electrocatalytic water oxidation. *Adv. Energy Mat.* **8,** 1703341 (2018).
17. Umena, Y. *et al*. Crystal structure of oxygen-evolving photosystem II at a resolution of 1.9 Å. *Nature* **473,** 55-60 (2011).
18. Kamiya, N. *et al*. Crystal structure of oxygen-evolving photosystem II from Thermosynechococcus vulcanus at 3.7-Å resolution. *PNAS* **100,** 98-103 (2003).
19. Zhu, D. *et al*. A 2D metal–organic framework/$Ni(OH)_2$ heterostructure for an enhanced oxygen evolution reaction. *Nanoscale* **11,** 3599-3605 (2019).
20. Liu, M. *et al*. Engineering bimetal synergistic electrocatalysts based on metal–organic frameworks for efficient oxygen evolution. *Small* **15,** 1903410 (2019).
21. Wang, B. *et al*. A general method to ultrathin bimetal-MOF nanosheets arrays via in situ transformation of layered double hydroxides arrays. *Small* **15,** 1804761 (2019).
22. Wang, H. *et al*. Metal-organic frameworks for energy applications. *Chem.* **2,** 52-80 (2017).
23. Li, W. *et al*. A bio-inspired coordination polymer as outstanding water oxidation catalyst via second coordination sphere engineering. *Nat. Commun.* **10,** 1-11 (2019).
24. Dogutan, D. K. *et al*. Electocatalytic water oxidation by cobalt (III) hangman β-octafluoro corroles. *J. Am. Chem. Soc.* **133,** 9178-9180 (2011).
25. Dong, J.-C. *et al*. Direct in situ Raman spectroscopic evidence of oxygen reduction reaction intermediates at high-index Pt (hkl) surfaces. *J. Am. Chem. Soc.* **142,** 715-719 (2019).
26. Mesbah, A. *et al*. From hydrated $Ni_3(OH)_2(C_8H_4O_4)_2(H_2O)_4$ to anhydrous $Ni_2(OH)_2(C_8H_4O_4)$: impact of structural transformations on magnetic properties. *Inorg. Chem.* **53,** 872-881 (2014).
27. Demadis, K. D. *et al*. Synthesis, structural characterization, and properties of new single and double cubanes containing the $MoFe_3S_4$ structural unit and molybdenum-bound polycarboxylate ligands. Clusters with a molybdenum-coordination environment similar to that in the iron-molybdenum cofactor of nitrogenase. *Inorg. Chem.* **34,** 436-448 (1995).
28. Luo, P. *et al*. In-situ growth of a bimetallic cobalt-Nickel organic framework on Iron foam: achieving the electron modification on a robust self-supported oxygen evolution electrode. *ChemCatChem.* **11,** 6061-6069 (2019).
29. Hammer, B. *et al*. Electronic factors determining the reactivity of metal surfaces. *Sur. Sci.* **1995,** *343*, 211-220.
30. Cai, Z. *et al*. Amorphous nanocages of Cu-Ni-Fe Hydr(oxy)oxide prepared by photocorrosion for highly efficient oxygen evolution. *Angew. Chem. Int. Ed.* **131,** 4233-4238 (2019).
31. Hong, W. T. *et al*. Charge-transfer-energy-dependent oxygen evolution reaction mechanisms for perovskite oxides. *Energy Environ. Sci.* **10,** 2190-2200 (2017).
32. Li, J. *et al*. Boosted oxygen evolution reactivity by igniting double exchange interaction in spinel oxides. *J. Am. Chem. Soc.* **142,** 50-54 (2019).

33. Jiang, J. *et al*. Atomic-level insight into super-efficient electrocatalytic oxygen evolution on iron and vanadium co-doped nickel (oxy) hydroxide. *Nature Commun.* **9,** 1-12 (2018).
34. Zeng, Q. *et al*. Role of ligands in catalytic water oxidation by mononuclear ruthenium complexes. *Coord. Chem.y Rev.* **304,** 88-101 (2015).
35. Wu, Q. *et al*. In situ coordination environment tuning of cobalt sites for efficient water oxidation. *ACS Catal.* **9,** 11734-11742 (2019).
36. Ji, Q. *et al*. Lattice strain induced by linker scission in metal–organic framework nanosheets for oxygen evolution reaction. *ACS Catal.* **10,** 5691 (2020).
37. Zhu, Y. *et al*. Boosting oxygen evolution reaction by creating both metal Ion and lattice-oxygen active sites in a complex oxide. *Adv. Mater.* **32,** 1905025 (2020).
38. Zhang, N. *et al*. Lattice oxygen activation enabled by high-valence metal sites for enhanced water oxidation. *Nat. Commun.* **11,** 1-11 (2020).
39. Liu, C. *et al*. Amorphous metal-organic framework-dominated nanocomposites with both compositional and structural heterogeneity for oxygen evolution. *Angew. Chem. Int. Ed.* **59,** 3630-3637 (2020).
40. Yang, C. *et al*. A. Phosphate ion functionalization of perovskite surfaces for enhanced oxygen evolution reaction. *J. Phys. Chem. Lett.* **8,** 3466-3472 (2017).
41. Shi, Y. *et al*. Unveiling the promotion of surface-adsorbed chalcogenate on the electrocatalytic oxygen evolution reaction. *Angew. Chem. Int. Ed.* **132,** 22656-22660 (2020).
42. Hollauer, E. *et al*. Fourier transform infrared and Raman spectra, vibrational assignment and ab initio calculations of terephthalic acid and related compounds. *Spectroc. Acta Pt. A-Molec. Biomolec. Spectr.* **57,** 993-1007 (2001).
43. Lee, M. W. *et al*. Infrared and Raman spectroscopic study of terephthalic acid adsorbed on silver surfaces. *J. Mol. Struct.* **415,** 93-100 (1997).
44. Jiang, J. *et al*. Bioinspired cobalt-citrate metal-organic framework as an efficient electrocatalyst for water oxidation. *ACS Appl. Mater. Interfaces.* **9,** 7193-7201 (2017).
45. Liang, R. *et al*. MIL-53 (Fe) as a highly efficient bifunctional photocatalyst for the simultaneous reduction of Cr(VI) and oxidation of dyes. *J. Hazard. Mater.* **287,** 364-372 (2015).

Figures

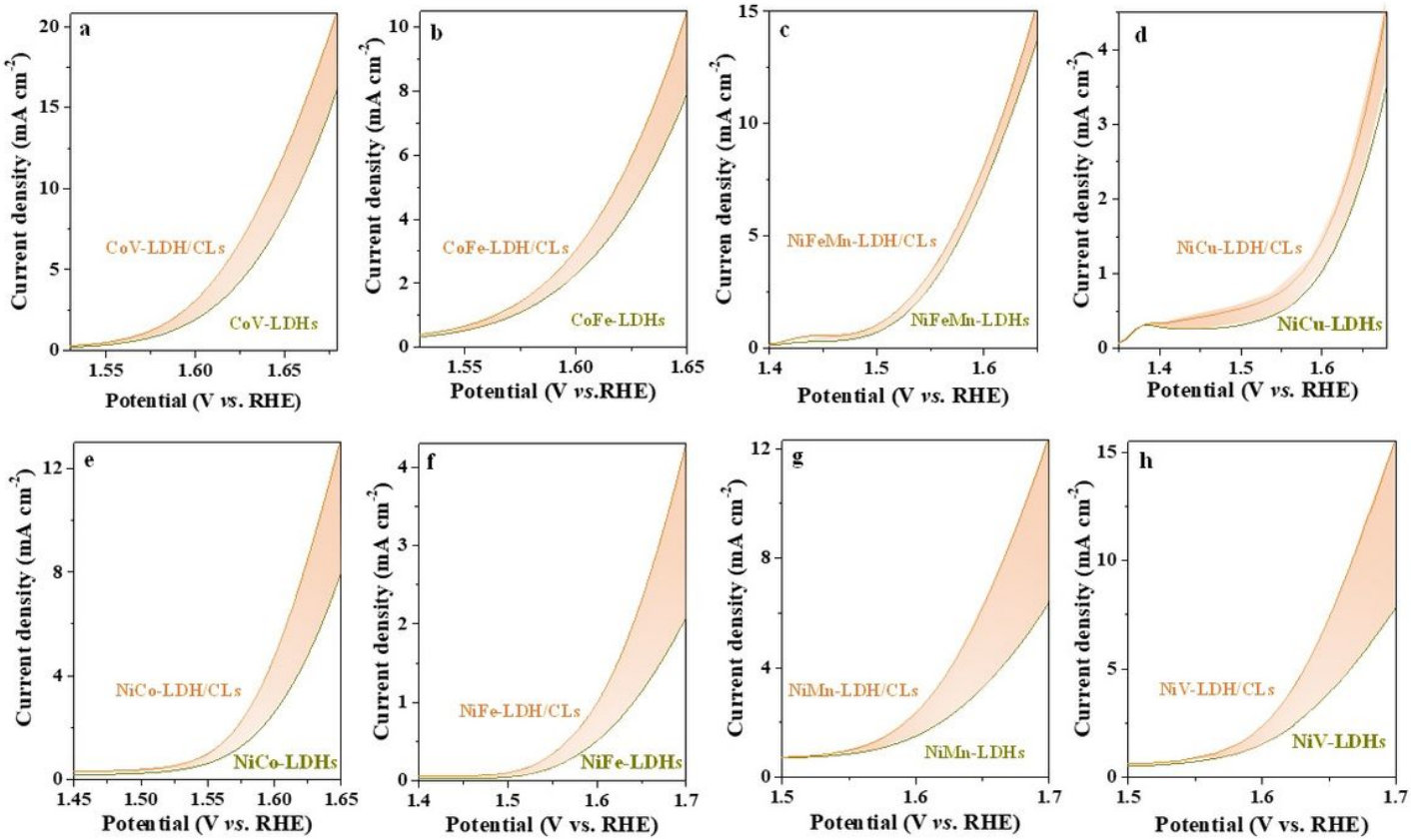

Figure 1

The liner sweep voltammetry curves of CoV-LDHs, CoFe-LDHs, NiFeMn-LDHs, NiCu-LDHs, NiCo- LDHs, NiFe-LDHs, NiMn-LDHs and NiV-LDHs in the electrolyte with and without CLs at PH = 14.

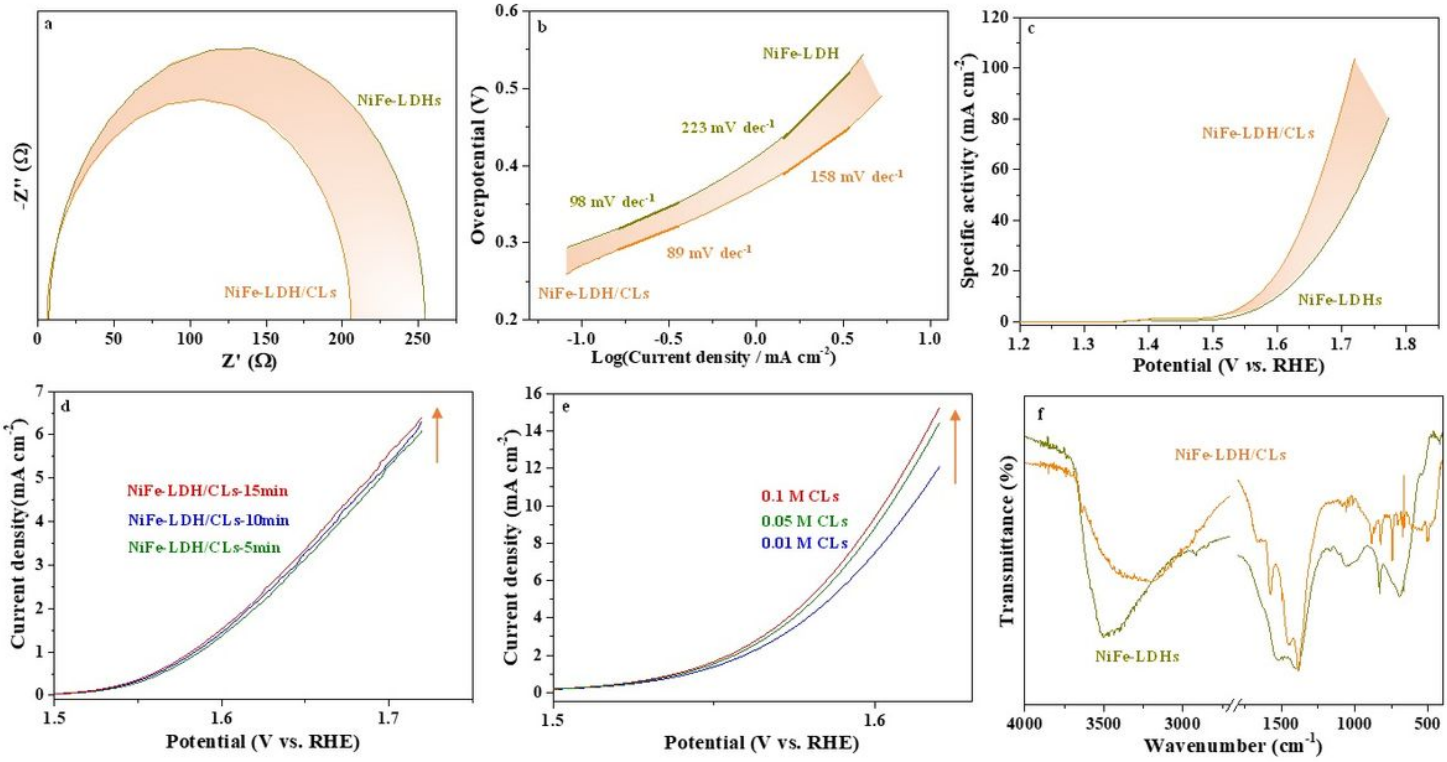

Figure 2

a) Nyquist plots, b) Tafel slopes, and c) LSVs of NiFe-LDHs in the electrolyte with and without CLs; d) LSVs of NiFe-LDHs with different soaking time in carboxylate-containing electrolyte; e) LSVs of NiFe-LDHs in the electrolyte with different concentrations of CLs; f) FT-IR spectroscopy of NiFe-LDHs in the electrolyte with and without CLs.

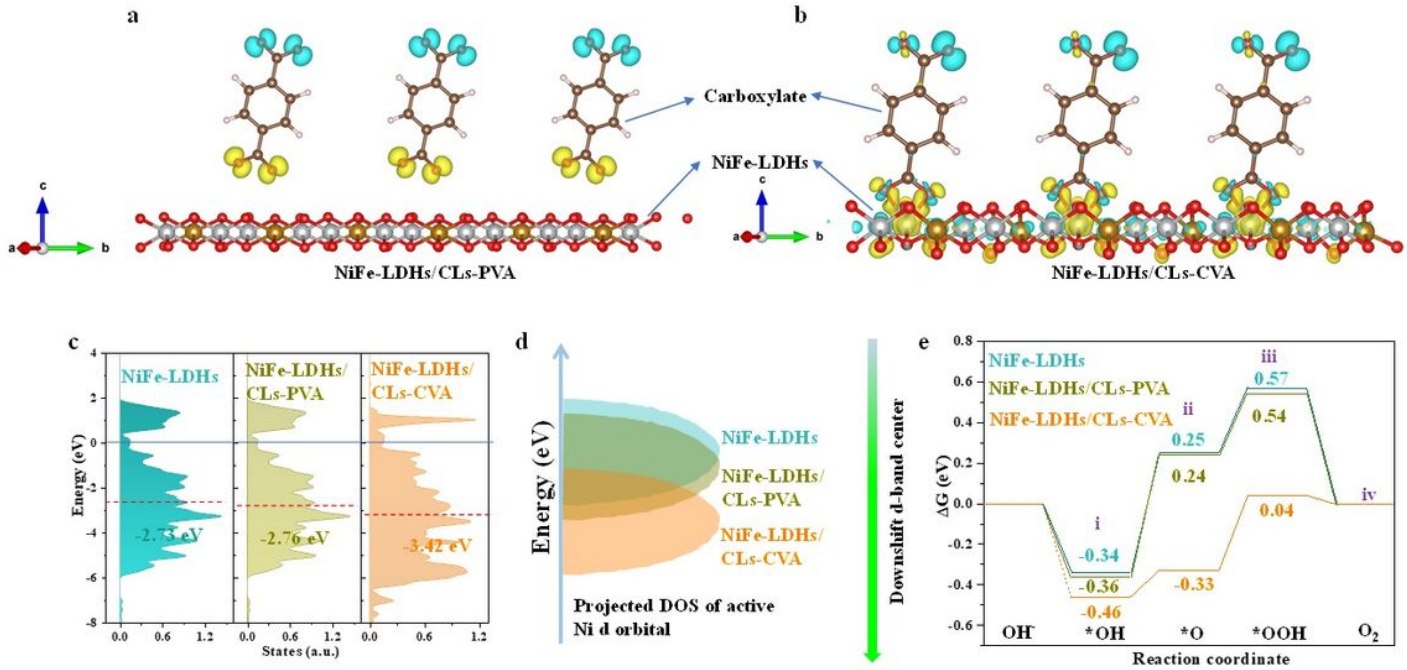

Figure 3

a) Differential charge densities of NiFe-LDHs/CLs-PVA; b) NiFe-LDHs/CLs-CVA theoretical models (yellow and cyan contours represens electron accumulation and depletion, respectively); c) The density of states (DOS) plots; d) Schematic of d-band center decreasing; e) Free-energy diagrams of NiFe-LDHs, NiFe-LDHs/CLs- PVA and NiFe-LDHs/CLs-CVA theoretical models.

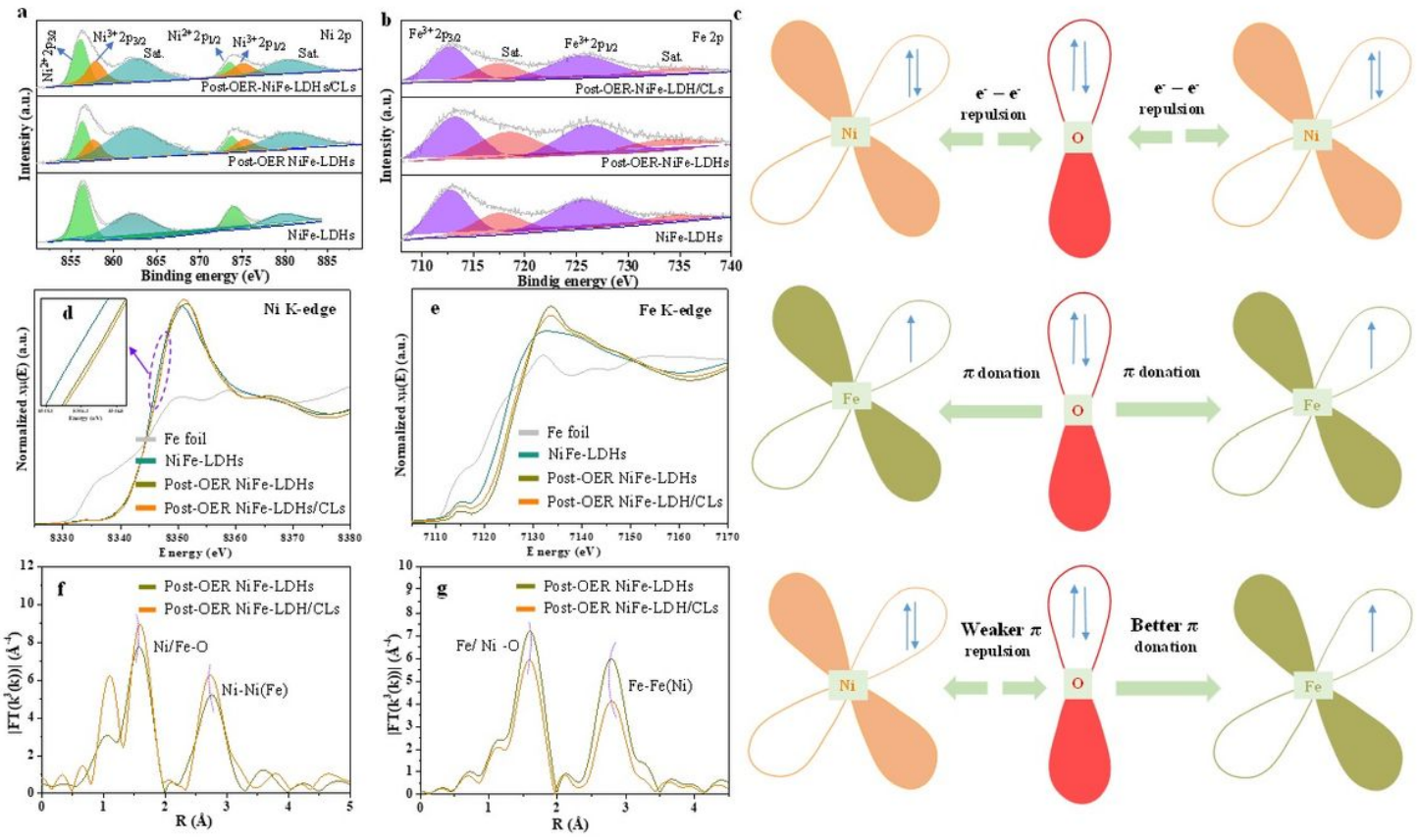

Figure 4

High-resolution XPS spectra of a) Ni 2p and b) Fe 2p for the NiFe-LDHs, post-OER NiFe-LDHs and post-OER NiFe-LDHs/CLs electrode; c) Schematic representation of the electronic coupling among Ni and Fe in post-OER NiFe-LDH/CL; d) Ni K-edge XANES; e) Fe K-edge XANES; f) Ni K-edge FT curves of the EXAFS k3χ(k) functions; g) Fe K-edge FT curves of the EXAFS k3χ(k) functions.

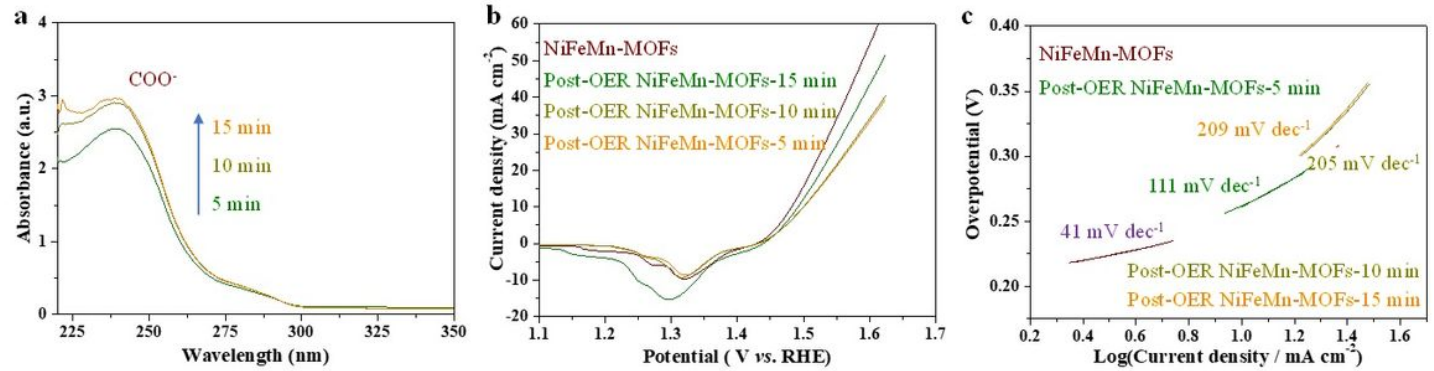

Figure 5

a) Uv-vis spectra of post-OER NiFeMn-MOFs at different soaking time in 6 M KOH; b and c) LSVs and corresponding Tafel curves of post-OER NiFeMn-MOFs-5, post-OER NiFeMn-MOFs-10 and post-OER NiFeMn- MOFs-15.

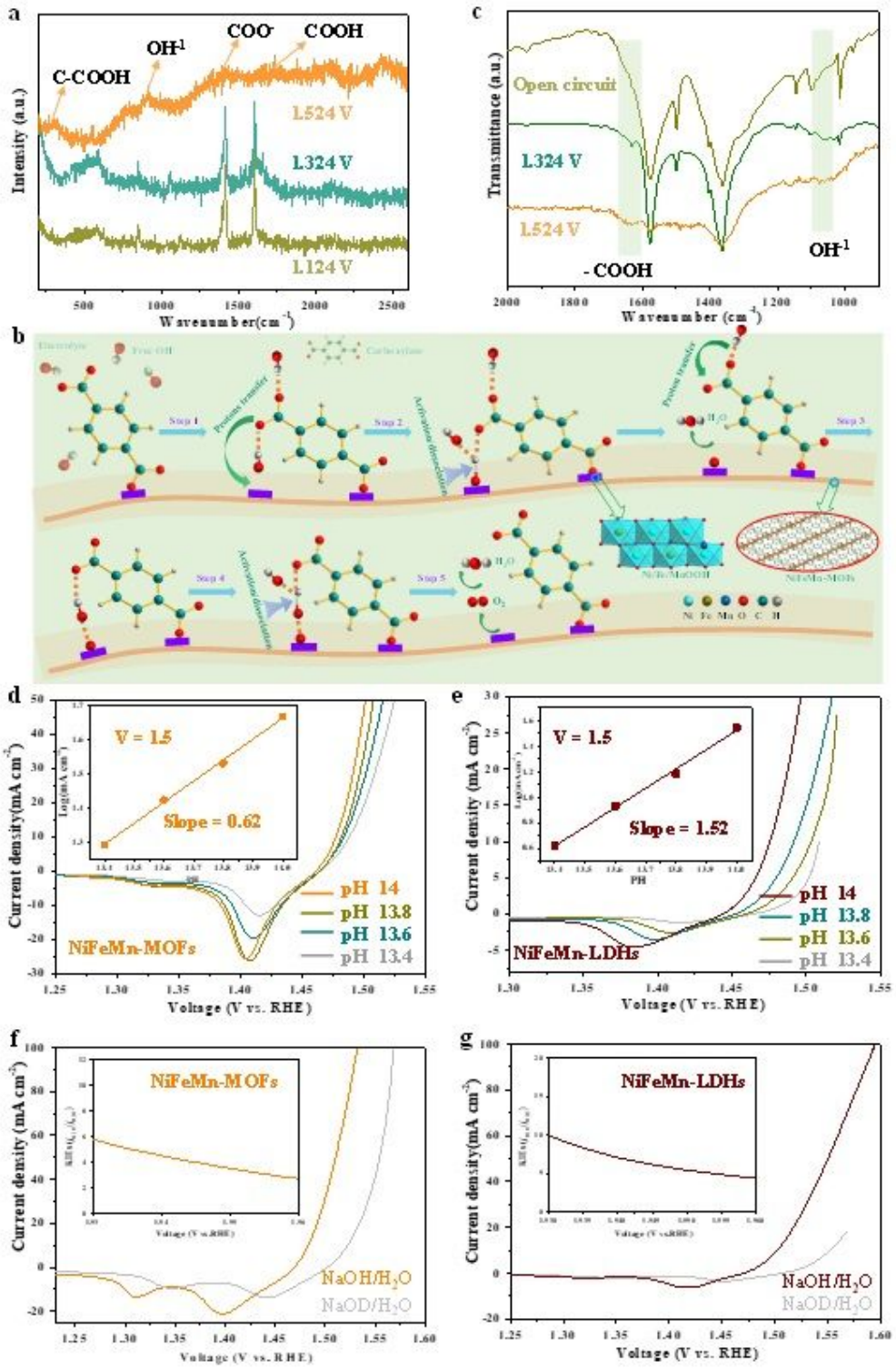

Figure 6

a) In situ Raman and FT-IR spectra of NiFeMn-MOFs; b) Schematic of proton transfer mediator and adsorption/activation/dissociation of OH-; c) In situ FT-IR spectra of NiFeMn-MOFs; d and e) LSVs of NiFeMn- MOFs and NiFeMn-LDHs at different pH values (the inset shows pH dependence); f) LSVs of NiFeMn-MOFs in aqueous 1.0 M NaOH and 1.0 M NaOD solutions (the inset is the kinetic isotope effect value vs potential).

Supplementary Files

This is a list of supplementary files associated with this preprint. Click to download.

- NiFeMIL53SI.docx
- Scheme1.pdf
- TableofContentsGraphic.jpg